Terahertz spin ratchet effect in magnetic metamaterials

M. Hild,[1] L. E. Golub,[1] A. Fuhrmann,[1] M. Otteneder,[1] M. Kronseder,[1] M. Matsubara,[2,3] T. Kobayashi,[2] D. Oshima,[4] A. Honda,[5] T. Kato,[4,5] J. Wunderlich,[1,6] C. Back,[7] and S. D. Ganichev[1,8]

[1]*Terahertz Center, University of Regensburg, 93040 Regensburg, Germany*
[2]*Department of Physics, Tohoku University, Sendai 980-8578, Japan*
[3]*Center for Science and Innovation in Spintronics, Tohoku University, Sendai 980-8577, Japan*
[4]*Department of Electronics, Nagoya University, Furo-cho, Chikusa-ku, Nagoya 464-8603, Japan*
[5]*Institute of Materials and Systems for Sustainability, Nagoya University, Furo-cho, Chikusa-ku, Nagoya 464-8603, Japan*
[6]*Institute of Physics ASCR, v.v.i., Cukrovarnická 10, 162 00 Prague 6, Czech Republic*
[7]*Technical University Munich, 85748 Garching, Germany*
[8]*CENTERA, Institute of High Pressure Physics PAS, 01142 Warsaw, Poland*

(Received 17 January 2023; revised 28 March 2023; accepted 30 March 2023; published 14 April 2023)

We report on spin ratchet currents driven by terahertz radiation electric fields in a Co/Pt magnetic metamaterial formed by triangle-shaped holes forming an antidot lattice and subjected to an external magnetic field applied perpendicularly to the metal film plane. We show that for a radiation wavelength substantially larger than the period of the antidots array, the radiation causes a polarization-independent spin-polarized ratchet current. The current is generated by the periodic asymmetric radiation intensity distribution caused by the near-field diffraction at the edges of the antidots, which induces spatially inhomogeneous periodic electron gas heating, and a phase-shifted periodic asymmetric electrostatic force. The developed microscopic theory shows that the magnetization of the Co/Pt film results in a spin ratchet current caused by both the anomalous Hall and the anomalous Nernst effects. Additionally, we observed a polarization-dependent trigonal spin photocurrent, which is caused by the scattering of electrons at the antidot boundaries resulting in a spin-polarized current due to the magnetization. Microscopic theory of these effects reveals that the trigonal photocurrent is generated at the boundaries of the triangle antidots, whereas the spin ratchet is generated due to the spatially periodic temperature gradient over the whole film. This difference causes substantially different hysteresis widths of these two currents.

DOI: 10.1103/PhysRevB.107.155419

I. INTRODUCTION

In a system with spatial asymmetry, carriers can perform a directed motion in response to ac electric fields or thermal/quantum fluctuations, i.e., when it is driven away from thermal equilibrium by an additional deterministic or stochastic perturbation. This directed transport, generally known as the ratchet effect, has a long history and is relevant for different fields of physics, chemistry, and biology; for reviews, see, e.g., Refs. [1–7]. Ratchet effects, whose prerequisites are simultaneous breaking of both thermal equilibrium and spatial inversion symmetry, can be realized in a great variety of forms. Examples range from mechanical systems and molecular motors to electric transport in one-dimensional (1D) semiconductor systems or metamaterials. Currently, ratchet systems already have fascinating ramifications in engineering and natural sciences. In metamaterials, conversion of high-frequency radiation into direct electric current due to the ratchet effect has been demonstrated in various two-dimensional semiconductor systems with periodic grating gate structures having an asymmetric configuration of the gate electrodes with period $d \ll \lambda$, where λ is the radiation wavelength [8–25]. Electric currents in response to a high-frequency electric field are detected in a wide range of temperatures (from room to helium temperatures) and frequencies (from tens of GHz to tens of THz) and can be excited both without and in the presence of an external magnetic field. In the latter case, it is called the magnetoratchet effect.

It has been shown theoretically [26] and demonstrated experimentally [27] that ratchet effects can also drive pure spin currents and spin-polarized electric currents. These types of ratchet effects were named spin ratchets. Spin ratchet effects, which can lead to novel ways for efficient generation and control of spin fluxes [28], attracted growing attention. Since the first work, several different origins of spin ratchet currents have been suggested and discussed [29–45]; for a review, see Ref. [46]. For example, it has been shown that a stationary spin current can be generated by applying an ac driving current to a symmetric or asymmetric periodic structure with Rashba spin-orbit coupling. Recently, the magnetoratchet effect resulting in a spin-polarized electric current has been excited by applying terahertz radiation to structures with an asymmetric double grating gate (DGG), lateral superlattices fabricated on a diluted magnetic semiconductor (DMS), and GaN two-dimensional electron systems [47–49]. The spin magnetoratchet is caused by spin-orbit interaction together with the action of a magnetic field resulting in the Zeeman effect, and it is expected to be substantially enhanced in DMS

materials with a lateral superlattice made of ferromagnetic materials. Note that in the latter case, a novel concept for a spin-transistor has been realized [50]. These works show that spin ratchet and spin transport in lateral superlattices may yield a potentially important basis for practical devices. Hereby, magnetic metamaterials made of ferromagnetic metals are good candidates for realizing spin ratchets.

Most recently, spin-sensitive currents have been observed in Co/Pt-based magnetic films with a lateral superlattice consisting of triangular antidots arising from excitation with visible and near-infrared light with $\lambda \approx d$ [51]. The dc current has been excited in individual triangles due to the magneto-photogalvanic effect [52]. Arrays of triangular and semidisk antidots in nonmagnetic materials fabricated on GaAs-based high-electron-mobility transistor structures were previously used to demonstrate the ratchet effect excited by high-frequency radiation with fulfilled condition $d \ll \lambda$ [53–57]. In this work, we used Co/Pt-based magnetic films with a lateral superlattice and extend the frequency range to terahertz (THz) radiation with a wavelength substantially larger than the period of the triangles, and we demonstrate that spin ratchets are efficiently excited in such structures in the absence, as well as in the presence, of an external magnetic field. We demonstrate that THz laser radiation results in a spin-polarized direct electric current consisting of two contributions: a polarization-independent ratchet current and a contribution whose direction and magnitude are determined by the orientation of the THz electric field (linear magnetic ratchet effect). We show that the application of an external magnetic field normal to the metal film results in a hysteretic behavior of both contributions to the ratchet current. We develop a theory that fully describes all experimental findings. We demonstrate that the polarization-dependent spin ratchet current appears due to the trigonal symmetry of the individual antidots. The polarization-insensitive photocurrent caused by the Seebeck ratchet [5] and spin ratchet effects become possible due to the reduced symmetry of the periodic structure as a whole, and they are absent in experiments with shorter wavelength satisfying the condition $\lambda \approx d$ [51]. The experimental data and the theoretical model are discussed by taking the asymmetric electrostatic potential profile and near-field effects explicitly into account. We show that the THz radiation-induced spin ratchet current appears in the triangular antidots superlattice due to the anomalous Nernst effect (ANE) and the anomalous Hall effect (AHE).

II. SAMPLE AND METHODS

Our samples were fabricated on a 4 mm×4 mm silicon dioxide (SiO_2) substrate and a silicon nitride (SiN) layer of 5 nm thickness. On top, a metallic cobalt/platinum (Co/Pt) multilayer film was deposited with a fivefold repeated stacking sequence of 0.5 nm Co and 0.9 nm Pt. This multilayer is embedded between two 2 nm Pt layers. We structured all Co and Pt layers with magnetron sputtering. The metallic layers have ferromagnetic properties with the easy axis perpendicular to the layers, i.e., in the growth direction z. Consequently, application of a magnetic field $\boldsymbol{H}$ that is greater than the coercive field along the z-axis results in a constant magnetization $\boldsymbol{M} \parallel z$ everywhere in the patterned film with perpendicular

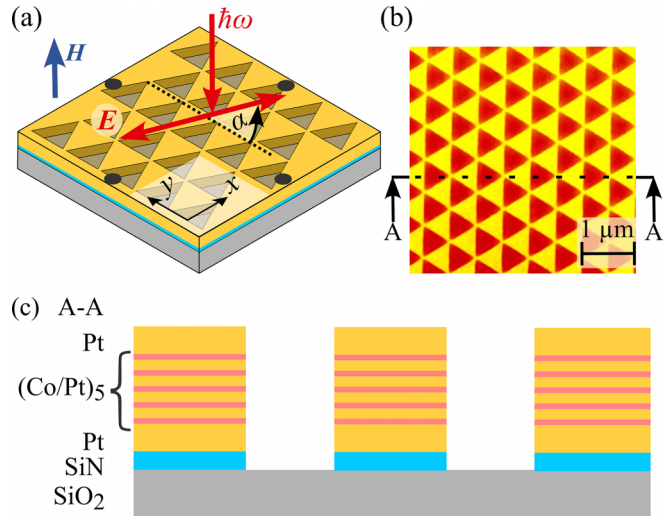

FIG. 1. Experimental setup (a), AFM image of the equilateral triangles (b), and cross-section (c) of the magnetic metamaterial formed by equilateral triangle-shaped antidots. Panel (a) shows the sample irradiated with linearly polarized light along the z-direction, i.e., normal to the sample surface. The red double arrow illustrates the radiation electric field vector $\boldsymbol{E}$ for linearly polarized radiation rotated anticlockwise by the azimuth angle α from the y-axis parallel to the triangle basis. Two pairs of Ohmic contacts allow us to probe the photocurrent excited in the x- and y-directions [58]. Note that the sketched triangles are enlarged for better visibility. A magnetic field $\boldsymbol{H}$ is applied along the z-axis. Panel (b) shows an AFM image of the array of the triangle-shaped antidots with a period 0.55 μm. Panel (c) sketches the structure cross-section by the A-A plane. It shows the layer stacking of the antidot lattice.

magnetic anisotropy. The key element is the array of equilateral, triangular holes forming an antidot lattice. We patterned this lattice in an area of 250 μm×250 μm by electron beam lithography and argon ion etching. The holes, about 20 nm in depth, have a side length of 480 nm, a period of 550 nm, and they are in the dimension of optical wavelengths. The cross-section of the layer sequence and the antidots of the manufactured sample is given in Fig. 1(c). The size of one antidot is slightly smaller than the spacing between them, so almost triangle-shaped metal parts are formed; see the atomic force microscope image presented in Fig. 1(b). For photoelectric and transport measurements, we made two pairs of Ohmic contacts orientated along the height (x-axis) and baseline (y-axis) of the triangles; see Figs. 1(a) and 10 in Appendix A. The measured magnetic field and temperature dependence of the two-point resistance is shown in Fig. 11 in Appendix A. It shows that the resistance at fixed temperature is independent of magnetic field in the field range used in the experiments ($|\mu_0 H| \leqslant 2$ T, where μ_0 is the vacuum permeability) and slightly increases by increasing the temperature from 120 to 300 K.

Figure 1(a) shows the experimental setup. The sample was excited by normally incident, linearly polarized radiation with a frequency of $f = 2.54$ THz, which corresponds to a wavelength of $\lambda = 118.8$ μm and photon energy of $\hbar\omega = 10.5$ meV. The THz radiation was generated by a cw methanol molecular gas laser optically pumped by a carbon dioxide

laser [59]. Laser radiation with power $P \approx 50$ mW was modulated by an optical chopper. The laser beam spot at the sample position was measured with a pyroelectric camera: it had an almost Gaussian beam profile with a full width at half-maximum of 1.8 mm. Subsequently, the radiation intensity on the sample was about $2\,\mathrm{W/cm^2}$. In two complementary experiments, we used high-power pulsed THz radiation with $\lambda = 90.5\,\mu\mathrm{m}$ ($f = 3.3$ THz) and cw infrared radiation $\lambda = 0.8\,\mu\mathrm{m}$. In the latter case, we used a cw Ti:sapphire laser with $200\,\mathrm{W\,cm^{-2}}$. In the former case, we used a pulsed optically pumped NH_3 laser with a pulse length of 100 ns and a peak intensity of $100\,\mathrm{kW\,cm^{-2}}$ [60,61]; both parameters are analyzed by photon drag [62] and photogalvanic [63] detectors. Depending on the wavelength, the beam spot diameter of the pulsed THz laser was from 1.5 to 3 mm, which was controlled by a pyroelectric camera [64].

In the experiments, the orientation of the radiation electric field vector $\boldsymbol{E}$ was rotated counterclockwise by the azimuth angle α with $\alpha = 0$ corresponding to $\boldsymbol{E} \parallel y$. For that, we used x-cut crystalline quartz half-wave plates. The photovoltage U_{ph} generated in the unbiased samples as a result of the excitation with cw radiation was amplified by a factor of 100 and measured applying standard lock-in technique. The photocurrent was calculated as $J = U_{\mathrm{ph}}/R_{\mathrm{s}}$, where R_{s} is the sample's resistance. In experiments with single-pulsed laser radiation, the signal was detected with a digital oscilloscope as a voltage drop over a load resistance $R_{\mathrm{L}} = 50\,\Omega$.

For studying photoelectric effects related to the magnetization in the magnetic metamaterial, a magnetic field $\boldsymbol{H}$ was applied normal to the structure plane. The measurements were performed in a wide range of temperatures from 100 to 300 K. For room-temperature measurements, a water-cooled electromagnet with $|\mu_0 H| \leqslant 0.4$ T was used. For low-temperature measurements, the samples were placed in an optical, temperature-variable magnetocryostat with z-cut crystal quartz windows. Here a magnetic field of $|\mu_0 H| = \pm 2$ T was obtained with a superconducting magnet. Additionally, we studied the magnetization curve of the unpatterned and patterned Co/Pt multilayer films using Faraday rotation measurements under illumination of 0.8 μm laser light [51].

III. RESULTS

We begin with the results obtained in the sample in a magnetic multidomain state, which was not subjected to any applied magnetic field before. Since the patterned film does not exhibit a globally constant magnetization, we assign the global magnetization $M = 0$ to this state. Irradiating the sample by THz radiation with $\lambda = 118\,\mu\mathrm{m} \gg d$ ($f = 2.54$ THz), we detected a signal that varies upon rotation of the radiation electric field vector $\boldsymbol{E}$. Figure 2(a) shows a polarization dependence for the photocurrent measured in the x- and y-directions. The data can be well fitted by

$$J_x = A_1 \cos 2\alpha + C_1, \tag{1}$$

$$J_y = -\tilde{A}_1 \sin 2\alpha + \tilde{C}_1. \tag{2}$$

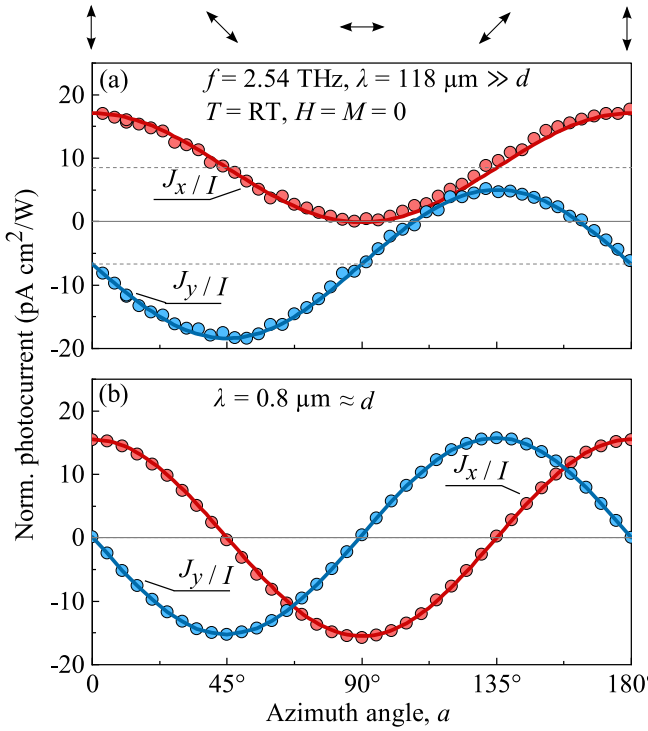

FIG. 2. Polarization dependencies of the photocurrents J_x (red circles) and J_y (blue circles) normalized to the radiation intensity I obtained for zero external magnetic field and magnetization, $\mu_0 H = M = 0$. Panel (a): photocurrents in response to the radiation with wavelength $\lambda = 118\,\mu\mathrm{m}$ much larger than the period of the antidots array $d = 0.55\,\mu\mathrm{m}$. The red solid line is a fit after Eq. (1) with fitting parameters $A_1 = 8.6\,\mathrm{pAcm^2}/W$ and $C_1 = 8.5\,\mathrm{pAcm^2}/W$. The blue solid line is a fit after Eq. (2) with fitting parameters $\tilde{A}_1 = 11.7\,\mathrm{pAcm^2}/W$ and $\tilde{C}_1 = -6.7\,\mathrm{pAcm^2}/W$. Dashed horizontal lines show the magnitudes of the polarization-independent offsets. Arrows on top illustrate the orientation of the radiation electric field vector for several values of α. Panel (b): photocurrents excited by radiation with $\lambda = 0.8\,\mu\mathrm{m} \approx d$. Red and blue curves are fits after Eqs. (1) and (2) with the fit parameters $A_1 = \tilde{A}_1$ and zero amplitudes of the polarization-independent contributions, $C_1 = \tilde{C}_1 = 0$.

The signal was also detected for a substantially smaller wavelength of $\lambda = 0.8\,\mu\mathrm{m} \approx d$, and its polarization dependence is also described by Eqs. (1) and (2); see Fig. 2(b). However, in this case no offsets were observed, so that $C_1 = \tilde{C}_1 = 0$. The photocurrent excited by $\lambda = 0.8\,\mu\mathrm{m} \approx d$ has recently been studied in detail in Ref. [51]. Therefore, in this paper we only briefly discuss this result and focus in the following on the photocurrent excited with $\lambda = 118\,\mu\mathrm{m} \gg d$.

The application of an external magnetic field $\boldsymbol{H}$ larger than the coercive field and normal to the metal layers results in a constant magnetization $\boldsymbol{M}$ everywhere in the patterned magnetic lattice and changes the polarization dependence of the signal [65]. It is shown in Fig. 3(a) that the photocurrent is now described by

$$J_x = A_1 \cos 2\alpha + C_1 + M_z(A_2 \sin 2\alpha + C_2). \tag{3}$$

Decomposing the polarization dependence into the odd and even part with respect to the magnetization M, we obtain

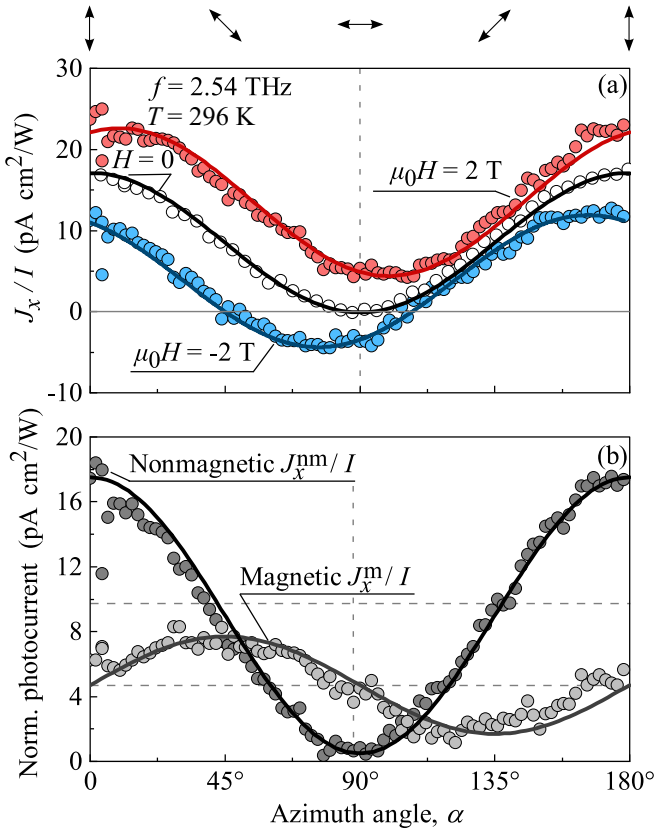

FIG. 3. Panel (a): Polarization dependencies of the photocurrent J_x normalized to radiation intensity I obtained for an external magnetic field $\mu_0 H = \pm 2$ T, red and blue circles, respectively. Black circles show J_x/I obtained for $\mu_0 H = M = 0$. Arrows on top illustrate the orientation of the radiation electric field vector for several values of α. The curves show fits after Eq. (3). Panel (b): Polarization dependence of the normalized nonmagnetic ($J_x^{\rm nm}$) and magnetic ($J_x^{\rm m}$) contributions obtained as the odd and even part with respect to the magnetization M_z induced by the magnetic field $\mu_0 H_z$; see Eqs. (4) and (5). The curves are fits after the first and second terms on the right-hand side of Eq. (3) (nonmagnetic photocurrent $J_x^{\rm nm}$) and the last two terms on the right-hand side of the same equation (magnetic photocurrent $J_x^{\rm m}$). Fit parameters are $A_1 = 8.5\,{\rm pAcm^2}/W$, $C_1 = 9\,{\rm pAcm^2}/W$, $A_2 = 3\,{\rm pAcm^2}/W$, and $C_2 = 5\,{\rm pAcm^2}/W$. Dashed horizontal lines show the magnitudes of the polarization-independent offsets.

the nonmagnetic $J_x^{\rm nm}$ and magnetic $J_x^{\rm m}$ contributions to the photocurrent:

$$J_x^{\rm nm} = \tfrac{1}{2}[J_x(+M_z) + J_x(-M_z)], \tag{4}$$

$$J_x^{\rm m} = \tfrac{1}{2}[J_x(+M_z) - J_x(-M_z)]. \tag{5}$$

The corresponding dependences are shown in Fig. 3(b) and confirm that the nonmagnetic and magnetic photocurrent contributions indeed vary as $\cos 2\alpha$ and $\sin 2\alpha$ functions, respectively. We emphasize that the $J_x^{\rm m}$ contribution has a magnetization-dependent offset, whereas the offset of $J_x^{\rm nm}$ does not depend on M_z.

Figure 4 shows the magnetic field dependence of the photocurrent. To describe individual contributions, we introduce the following notation. To distinguish the nonmagnetic and

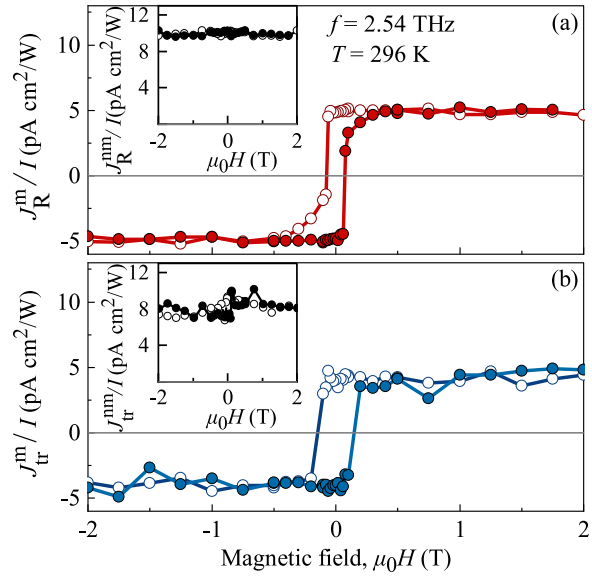

FIG. 4. Magnetic-field dependence of the magnetization-induced polarization-independent [panel (a)] and polarization-dependent [panel (b)] photocurrent contributions measured in the x-direction and normalized to the radiation intensity. Following Eq. (3), these contributions are defined as $J_{\rm R}^{\rm m} = M_z A_2 \sin 2\alpha$ and $J_{\rm tr}^{\rm m} = M_z C_2$. Each point has been extracted from a measured α-dependence at a constant magnetic field. Full and empty circles show the forward and backward magnetic field sweeps, respectively. Insets in panels (a) and (b) show magnetic field dependencies of the normalized $J_{{\rm R},x}^{\rm nm} = C_1$ and $J_{{\rm tr},x}^{\rm nm} = A_1 \cos 2\alpha$, respectively. The inset demonstrates that they are independent of the magnetic field for both magnetic field sweep directions.

magnetic photocurrent contributions, we used the superscripts "nm" and "m," respectively. The polarization-independent offsets are quoted as $J_{\rm R}^{\rm nm}$ and $J_{\rm R}^{\rm m}$, whereas the polarization-dependent parts are given by $J_{\rm tr}^{\rm nm}$ and $J_{\rm tr}^{\rm m}$. The subscripts "R" and "tr" indicate the ratchet and the trigonal photocurrent mechanisms, which, as we show below, are responsible for the polarization-independent offset and the polarization-dependent part, respectively. The polarization-dependent and -independent parts of the photocurrent were obtained from azimuth angle dependences measured for each magnetic field.

The insets in Figs. 4(a) and 4(b) demonstrate that the magnetization-even contributions are independent of the magnetic field in the studied range from -2 to 2 T. In contrast, the magnetization-odd parts exhibit a clear hysteresis for $|\mu_0 H| < 0.3$ T, whereas at higher H-fields they do not depend on magnetic field and have opposite polarities for positive and negative H; see Figs. 4(a) and 4(b) [66]. Photocurrents at high magnetic fields, $|\mu_0 H| > 0.3$ T, were studied to examine the presence of a possible Hall contribution caused by the external magnetic field. In this case, the curves will show a linear increase of the signal after the magnetization saturation. Our data show that after the magnetization saturation, the amplitude of the photocurrent does not depend on B, which rules out a simple change of the current magnitude due to the Hall effect. Thus, the whole discussion of magneto-photocurrent is reduced to the magnetization-induced effects. The amplitude of the photocurrent at fields corresponding the

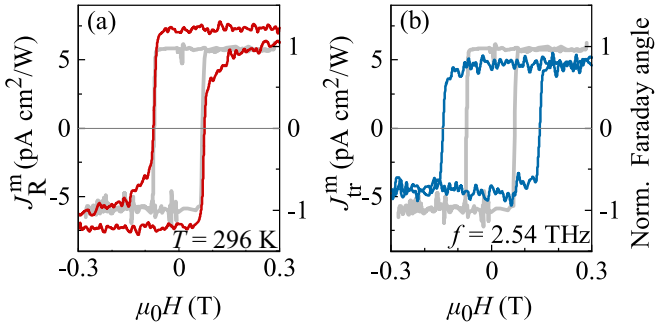

FIG. 5. Zoom of the hysteretic parts of the magnetic field dependencies of J_R^m/I [panel (a)] and J_{tr}^m/I [panel (b)] presented in Fig. 4. The gray curves show the magnetic field dependence of the Faraday rotation angle measured in the unpatterned Co/Pt multilayer film. The angles are normalized to the maximum; see the right axis.

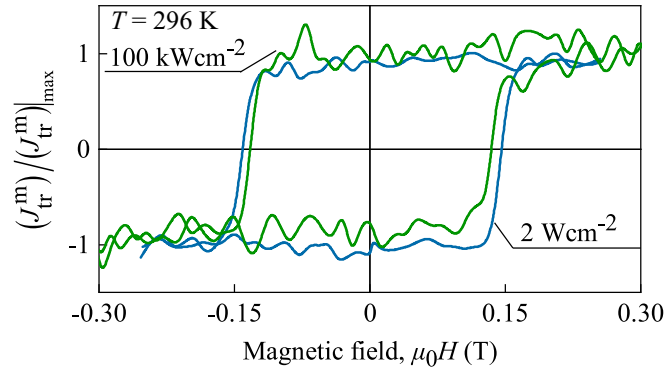

FIG. 6. Magnetic-field dependence of the magnetization-induced polarization-dependent photocurrent contribution measured in the x-direction at low (blue trace) and high (green trace) radiation intensities. Each curve is normalized to the signal maximum, $(J_{tr}^m)/(J_{tr}^m)|_{max}$. The blue curve has been obtained with THz radiation of a cw laser operating at a frequency $f = 2.54$ THz and intensity $I = 2\,\mathrm{W\,cm^{-2}}$, and the green one with radiation from a pulsed laser operating at a frequency $f = 3.33$ THz and $I = 100\,\mathrm{kW\,cm^{-2}}$. The plot reveals that both curves have almost the same hysteresis width despite the almost five orders of magnitude difference in the radiation intensity.

magnetization saturation is almost independent of temperature for $T \gtrsim 100$ K (not shown).

Figures 5(a) and 5(b) show the hysteretic part of the magnetic field dependence for the photocurrent contributions J_R^m and J_{tr}^m, respectively. They also display the magnetic field dependence of the Faraday rotation angle $\theta \propto M$; see the gray lines in Fig. 5. These measurements were performed on the unpatterned Co/Pt multilayer film using linearly polarized radiation of $\lambda = 118\,\mu$m passing through the magnetic material. Figure 5 demonstrates that the hysteresis width of the polarization-independent contribution J_R^m is the same as the one of the magnetization, whereas the hysteresis width of the polarization-dependent part J_{tr}^m is somewhat larger than that of M. This is most clearly seen in panel (d) of Fig. 12 in Appendix B where the photocurrent contributions $\propto J_R^m$ and $J_{tr}^m \sin 2\alpha$ at $\alpha = 135^\circ$ have opposite signs. Last but not least, by performing measurements at almost five orders of magnitude higher intensities, we obtained that while the magnitude of the photocurrent drastically increases, the hysteresis width of the polarization-dependent photocurrent J_{tr}^m remains unchanged; see Fig. 6.

IV. THEORY OF PHOTOCURRENTS FORMED IN ISOLATED EQUILATERAL TRIANGLE-SHAPED ANTIDOTS

In the metal layers forming the studied samples, the normally incident radiation can excite the photocurrent only in the antidots array because a photocurrent in the unpatterned part of the sample is forbidden by symmetry. For a wavelength λ smaller than or comparable to the period d, the photocurrent generation should be considered for isolated triangles, whereas for the opposite limit ($\lambda \gg d$) the antidots array should be treated as a metamaterial. As we show below (Sec. V), in the latter case the photocurrent is caused by the ratchet effect, which additionally gives rise to polarization-independent photocurrents detected in our experiments applying radiation with $\lambda = 118\,\mu$m. Below we develop the phenomenological and microscopic theory for the polarization-dependent photocurrent excited in the isolated triangles.

A. Phenomenology

For the photocurrent formed due to scattering by individual triangular antidots, the actual point group symmetry is C_{3v}. This is the group symmetry of an equilateral triangle with three reflection planes oriented at 120° to each other. This symmetry consideration yields the following relations between the photocurrent density [67], magnetization, and radiation polarization parameters:

$$j_x = \chi P_{\mathrm{lin}} E_0^2 + M_z \Phi P'_{\mathrm{lin}} E_0^2,$$
$$j_y = -\chi P'_{\mathrm{lin}} E_0^2 + M_z \Phi P_{\mathrm{lin}} E_0^2. \quad (6)$$

Here E_0 is the amplitude of the radiation electric field $\boldsymbol{E} = E_0 \boldsymbol{e} \exp(-i\omega t) + \mathrm{c.c.}$, with $\boldsymbol{e}$ being the polarization unit vector, Φ and χ are constants, and the axes (x, y) are related to the main axes of the C_{3v} point group: one of the three reflection planes is chosen as (zx). The Stokes parameters of radiation P_{lin} and P'_{lin} are the linear degrees:

$$P_{\mathrm{lin}} = |e_x|^2 - |e_y|^2, \quad P'_{\mathrm{lin}} = e_x e_y^* + e_x^* e_y. \quad (7)$$

In our experiments applying linearly polarized radiation they vary with the azimuth angle α as

$$P_{\mathrm{lin}} = \cos 2\alpha, \quad P'_{\mathrm{lin}} = \sin 2\alpha. \quad (8)$$

We see that the polarization-dependent photocurrent components in C_{3v} symmetry have π-periodic dependence on the polarization plane orientation. This is caused by the measurement setup where the j_x and j_y components are detected, i.e., the currents in the reflection plane (zx) and perpendicular to it. If, otherwise, the contacts are deposited along the pair of axes rotated by an angle Ψ to x, y, then the additional phase 3Ψ appears in the expressions for the photocurrents, which reflects the trigonal symmetry of the system [68,69].

B. Magnetization-independent trigonal photocurrent

The magnetization-independent photocurrent described by the constant χ in Eqs. (6) is the "trigonal" linear photogalvanic effect (LPGE) current $\boldsymbol{j}^{\rm tr}$. It is present due to asymmetrical scattering and has been studied in detail in intrinsically trigonal systems [68–72]. The system under study is extrinsically trigonal because of the presence of the artificially made macroscopic triangle antidots. Assuming rare electron scattering on triangle antidot boundaries, the trigonal current can be derived from the Boltzmann kinetic equation, which reads

$$\frac{df_{\boldsymbol{p}}}{dt} + e\boldsymbol{E}\cdot\frac{df_{\boldsymbol{p}}}{d\boldsymbol{p}} = \sum_{\boldsymbol{p}'}(W_{\boldsymbol{p}\boldsymbol{p}'}f_{\boldsymbol{p}'} - W_{\boldsymbol{p}'\boldsymbol{p}}f_{\boldsymbol{p}}). \tag{9}$$

Here $f_{\boldsymbol{p}}$ is the electron distribution function, $\boldsymbol{p}$ is the electron momentum, and $W_{\boldsymbol{p}'\boldsymbol{p}}$ is the probability of the elastic scattering process $\boldsymbol{p}\to\boldsymbol{p}'$. The scattering probability is conveniently decomposed into the symmetric and asymmetric parts with respect to the interchange of initial and final momenta:

$$W_{\boldsymbol{p}'\boldsymbol{p}} = W^{(s)}_{\boldsymbol{p}'\boldsymbol{p}} + W^{(a)}_{\boldsymbol{p}'\boldsymbol{p}}, \quad W^{(s,a)}_{\boldsymbol{p}\boldsymbol{p}'} = \pm W^{(s,a)}_{\boldsymbol{p}'\boldsymbol{p}}. \tag{10}$$

The symmetrical part $W^{(s)}_{\boldsymbol{p}'\boldsymbol{p}}$ determines the relaxation times of different Fourier-harmonics of the distribution function, τ_n ($n = 1, 2, \ldots$):

$$\tau_n^{-1} = \sum_{\boldsymbol{p}'} W^{(s)}_{\boldsymbol{p}'\boldsymbol{p}}(1-\cos n\theta_{\boldsymbol{p}\boldsymbol{p}'}), \tag{11}$$

where $\theta_{\boldsymbol{p}\boldsymbol{p}'}$ is the angle between $\boldsymbol{p}$ and $\boldsymbol{p}'$ [68]. In particular, τ_1 is the transport relaxation time, and τ_2 is the relaxation time for the momentum-aligned electron distribution.

Taking into account the asymmetric part in linear order, we obtain the trigonal photocurrent described by the constant χ in Eqs. (6), where [72]

$$\chi = -\frac{2Ne^3\tau_1}{m\varepsilon_{\rm F}\left(1+\omega^2\tau_1^2\right)} \times\left[\frac{d(\xi_{\rm tr}v_{\rm F}\varepsilon_{\rm F}\tau_2)}{d\varepsilon_{\rm F}} - \frac{d\tau_1}{d\varepsilon_{\rm F}}\frac{\tau_2}{\tau_1}\xi_{\rm tr}v_{\rm F}\frac{1-\omega^2\tau_1\tau_2}{1+\omega^2\tau_2^2}\right]. \tag{12}$$

Here N is the 2D electron concentration, m is the effective mass, $\varepsilon_{\rm F}$ and $v_{\rm F}$ are the Fermi energy and velocity, $\tau_{1,2}$ are taken at the Fermi energy, and the dimensionless parameter $\xi_{\rm tr}$ accounts for the trigonal scattering asymmetry:

$$\xi_{\rm tr} = \tau_1\sum_{\boldsymbol{p}'}\left\langle W^a_{\boldsymbol{p}\boldsymbol{p}'}\cos 2\varphi_{\boldsymbol{p}'}\cos\varphi_{\boldsymbol{p}}\right\rangle_{\varphi_{\boldsymbol{p}}}. \tag{13}$$

Here angular brackets denote averaging over directions of the momentum $\boldsymbol{p}$ at a fixed energy $\varepsilon_{\rm F}$, and $\varphi_{\boldsymbol{p}}, \varphi_{\boldsymbol{p}'}$ are polar angles of the corresponding momenta. For a particular case of scattering by short-range impurities, we have

$$\xi_{\rm tr} = 2\pi g_0 V_0\langle F_{\boldsymbol{p}\boldsymbol{k}\boldsymbol{p}'}\cos 2\varphi_{\boldsymbol{p}'}\cos\varphi_{\boldsymbol{p}}\rangle_{\varphi_{\boldsymbol{p}},\varphi_{\boldsymbol{p}'},\varphi_{\boldsymbol{k}}}. \tag{14}$$

Here g_0 is the density of states at the Fermi energy, V_0 is the scattering amplitude by impurities, and $F_{\boldsymbol{p}\boldsymbol{k}\boldsymbol{p}'} = \langle u_{\boldsymbol{p}}|u_{\boldsymbol{p}'}\rangle\langle u_{\boldsymbol{p}'}|u_{\boldsymbol{k}}\rangle\langle u_{\boldsymbol{k}}|u_{\boldsymbol{p}}\rangle$ is a product of the Bloch amplitude overlaps.

The considered microscopic mechanism of the trigonal photocurrent $\boldsymbol{j}^{\rm tr}$ formation is illustrated in Figs. 7(a) and 7(b). In general, scattering of electrons in a metal at the antidot boundaries violates the detailed equilibrium giving rise to the asymmetrical part of the scattering probability. In equilibrium, i.e., without any external influence, the scattering, obviously, does not result in an electric current. In the presence of radiation, however, the electron distribution is aligned in momenta along the radiation electric field. Formally, it means that a correction $\delta f_{\boldsymbol{p}} \propto \tau_2 E_0^2\cos 2\varphi_{\boldsymbol{p}}$ appears as a solution of the Boltzmann Eq. (9) in the second order in the radiation electric field where only the symmetrical part of the scattering probability $W^{(s)}_{\boldsymbol{p}\boldsymbol{p}'}$ is taken into account. Then accounting for the asymmetrical part, i.e., scattering by the antidots, we see from Figs. 7(a) and 7(b) that a directed flow of electrons is formed with a direction governed by the radiation polarization. The resulting current direction depends on the relative orientation of the radiation electric field and the antidot: e.g., the field parallel to the triangle base, see Fig. 7(a), yields a current flowing in the x-direction, while rotation of the electric field by 90° reverses the current direction; see Fig. 7(b). The corresponding dependencies of the photocurrents on the electric field vector orientation are given for j_x and j_y by the first terms on the right-hand sides of Eqs. (6).

We note that the trigonal photocurrents discussed so far for nonmagnetic bulk semiconductors [70,73–75] and two-dimensional systems [53,57,71,72,76,77] have been observed experimentally and considered theoretically in terms of spin-independent mechanisms only. The only material in which the formation of the photocurrent without magnetization or without an external magnetic field involves spin was 3D topological insulators. In these materials, the trigonal current is generated in the topologically protected surface states [68,69,78–82]. Here spin-momentum locking should be considered in the current generation processes, and it causes the spin polarization of the photocurrent.

C. Magnetization-induced trigonal photocurrent

A magnetic field applied along the z-direction, which causes the magnetization M_z, gives rise to new photocurrent contributions, which can be excited by linearly as well as circularly polarized radiation; see the second and third terms on the right-hand sides of Eqs. (6), respectively. We develop a microscopic theory of the former effect and find the corresponding constant Φ. We propose and analyze three microscopic mechanisms based on (i) the anomalous Hall effect (AHE), (ii) spin-dependent scattering, and (iii) magnetization-dependent scattering. Since all detected photocurrents have hysteretic behavior and saturate at large positive and negative magnetic fields, see Fig. 4, they are determined solely by the magnetization M_z, while the effects of the Lorentz force, resulting in the linear in H_z dependence, are negligible.

1. Anomalous-Hall-effect–induced trigonal photocurrent

First, we consider the photocurrent contribution caused by the anomalous Hall effect. As is well known in the presence of magnetization, any dc electric current acquires a perpendicular component. In the experiments considered, this results in a component $\boldsymbol{j}\propto\boldsymbol{j}^{\rm tr}\times\boldsymbol{M}$ perpendicular to the trigonal LPGE current $\boldsymbol{j}^{\rm tr}$. Microscopically, there are both intrinsic and extrinsic contributions to the AHE, and the most efficient one is

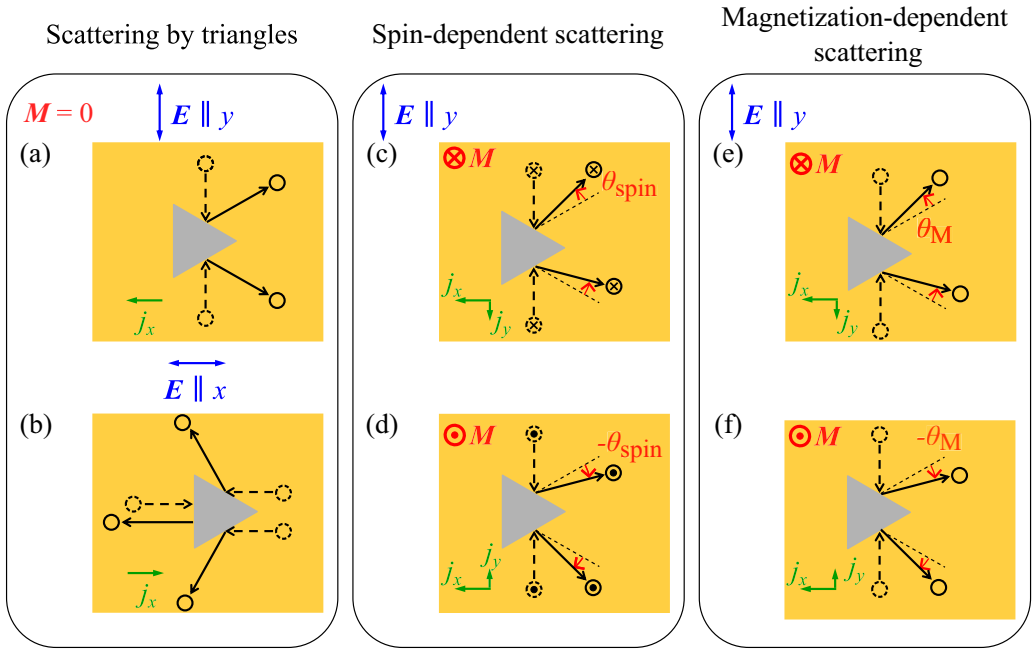

FIG. 7. Microscopic models for the trigonal photocurrents excited in equilateral triangle-shaped antidots. The field $\boldsymbol{E}$ results in a directed motion of carriers shown by the dashed arrows. This is described by the stationary correction to the distribution function $f_{\boldsymbol{p}}^{(2)} \propto |\boldsymbol{E}|^2$ being *second order* in the electric field. Due to asymmetric scattering, a directed carrier flow and, therefore, an electric current j is generated. Panels (a) and (b) show the dc current generation for zero magnetization and two directions of the radiation electric field resulting in the momentum alignment along the y- and x-directions, respectively; see Sec. IV B. Each column represents a different mechanism, as indicated by the heading on top. In (a), as a consequence of the external electric field $\boldsymbol{E} \parallel y$, electrons predominantly scatter along the x-axis (solid arrows), which results in an electric current in the x-direction. Rotation of the electric field by 90°, panel (b), reverses the direction of the predominantly scattered electrons; consequently, the electric current changes its sign. The electric field orientation dependence of the dc current j_x is given by $\cos(2\alpha)$; see Eqs. (6) and (8). Panels (c) and (d) illustrate the deflection of the electron trajectory by an angle $\theta_{\rm spin}$ caused by the spin polarization of the carriers due to the out-of-plane magnetization M_z; see Sec. IV C 2. This process results in the emergence of a spin-polarized photocurrent $j_y \propto M_z$, which reverses its sign upon switching the magnetization direction, as shown in panels (c) and (d) for $\pm M_z$. Panels (e) and (f) show the deflection of the electron trajectory by an angle $\theta_{\rm M}$ due to magnetization-dependent scattering; see Sec. IV C 3. This mechanism does not require spin polarization and also results in a photocurrent $j_y \propto M_z$.

usually caused by skew-scattering on impurities. In this mechanism, the magnetization-dependent photocurrent is given by

$$\boldsymbol{j} = \xi_{\rm AHE} P_s \boldsymbol{j}^{\rm tr} \times \hat{\boldsymbol{z}}. \tag{15}$$

Here P_s is the electron spin polarization, which appears due to the Zeeman effect,

$$P_s = -\frac{\Delta_Z}{2\varepsilon_{\rm F}} \propto M_z, \tag{16}$$

with Δ_Z being the Zeeman splitting, and the dimensionless skew scattering efficiency $\xi_{\rm AHE}$ given by [83]

$$\xi_{\rm AHE} = \tau_1 \left\langle \sum_{\boldsymbol{p}'} \sin(\varphi_{\boldsymbol{p}} - \varphi_{\boldsymbol{p}'}) W_{\boldsymbol{p}'\boldsymbol{p}}^{(a,{\rm SO})} \right\rangle_{\varphi_{\boldsymbol{p}}}. \tag{17}$$

Equation (15) agrees with the phenomenological Eqs. (6) yielding $\Phi M_z = \xi_{\rm AHE} P_s \chi$. Note that this mechanism requires a double account for the scattering asymmetry: at the first stage where the constant χ is obtained, Eq. (12), and at the second stage, at a deflection of the trigonal current. Even though each asymmetrical scattering probability can be obtained beyond the Born approximation only, in the Co-based structure with strong AHE this photocurrent formation mechanism can be of equal importance or even dominate over the other mechanisms considered below.

2. *Spin-dependent scattering-induced trigonal photocurrent*

The skew scattering considered above is also responsible for a further contribution that comes from spin-dependent electron scattering on triangle boundaries. Due to spin-orbit interaction, spin-up and spin-down electrons scatter off the antidot boundaries with an angle $\pm\theta_{\rm spin}$ with respect to the spinless case; see Figs. 7(c) and 7(d). Due to the spin polarization caused by the magnetization, Eq. (16), the majority of electrons having spin-up (spin-down) will be preferentially deflected up (down) by the angle $\theta_{\rm spin}$ ($-\theta_{\rm spin}$) relative to the nonmagnetized situation; see Fig. 7(c) [Fig. 7(d)]. This process results in the generation of a magnetic-field-dependent photocurrent that is rotated relative to the previously considered trigonal LPGE current $\boldsymbol{j}^{\rm tr}$ formed at $M_z = 0$. For example, at vertical polarization the component $j_y \propto M_z$ emerges, while in the nonmagnetic case the trigonal current $\boldsymbol{j}^{\rm tr}$ flows parallel to the x-direction; cf. Figs. 7(c) and 7(d). Reversing the magnetization M changes the sign of the j_y photocurrent component. This consideration fully agrees with the

phenomenological Eqs. (6) yielding the photocurrent given by the constant Φ.

Microscopically, the photocurrent density $j_{x,y} \propto M_z\Phi$ can be derived from the kinetic Eq. (9) similarly to the trigonal photocurrent. Assuming rare electron scattering on the triangle boundaries, we obtain that $M_z\Phi$ is given by Eq. (12) with two substitutions:

$$N \to P_s N, \quad \xi_{\rm tr} \to \xi_{\rm SO}. \tag{18}$$

Here the spin-orbit scattering asymmetry factor $\xi_{\rm SO}$ is given by

$$\xi_{\rm SO} = \tau_1 \left\langle \sum_{\boldsymbol{p}'} \sin\varphi_{\boldsymbol{p}} \cos 2\varphi_{\boldsymbol{p}'} W^{(a,{\rm SO})}_{\boldsymbol{p}'\boldsymbol{p}} \right\rangle_{\varphi_{\boldsymbol{p}}}, \tag{19}$$

where $W^{(a,{\rm SO})}_{\boldsymbol{p}'\boldsymbol{p}}$ is the asymmetric scattering probability calculated with an account for the spin-orbit interaction in the electron Bloch amplitudes; cf. Eq. (14).

3. Magnetization-dependent scattering-induced trigonal photocurrent

Magnetization not only results in the spin polarization of electrons considered above, but it also affects the electron orbital motion. Thus, electrons are scattered off the antidot boundaries at an additional angle θ_M, which is the same for spin-up and spin-down electrons, but reverses its sign upon switching the magnetization direction; see Figs. 7(e) and 7(f). As a result, an additional contribution to the photocurrent $j \propto M_z$ is generated. For the vertical polarization, it corresponds to $\pm j_y$; see Figs. 7(e) and 7(f).

Microscopically this contribution is obtained if one accounts for the magnetization in the Bloch amplitudes. This yields the asymmetrical scattering probability $W^{(a,M)}_{\boldsymbol{p}'\boldsymbol{p}}$ dependent on M_z. The value of $M_z\Phi$ in this mechanism is given by Eq. (12) with the magnetization-induced factor

$$\xi_M = \tau_1 \left\langle \sum_{\boldsymbol{p}'} \sin\varphi_{\boldsymbol{p}} \cos 2\varphi_{\boldsymbol{p}'} W^{(a,M)}_{\boldsymbol{p}'\boldsymbol{p}} \right\rangle_{\varphi_{\boldsymbol{p}}}. \tag{20}$$

The value ξ_M is odd in M_z and it is linear in the magnetization to the lowest order.

V. THEORY OF RATCHET CURRENT IN ANTIDOT MAGNETIC METAMATERIALS

Previously we considered the photocurrent generation caused by the individual triangle antidots. Each triangle has C_{3v} symmetry with three reflection planes and the C_3 axis. As we demonstrated above, in this case the photocurrents j_x and j_y are solely defined by the degree of linear polarization given by the corresponding Stokes parameters $P_{\rm lin}$ and $P'_{\rm lin}$. For a wavelength larger than the period of the array of the triangle antidots forming a lateral superlattice, however, large polarization-independent photocurrent contributions are detected. This observation indicates the symmetry reduction due to the absence of two or even all three reflection planes, meaning the point symmetry group C_s or C_1, respectively. In the former case, the reflection plane (zx) is the only nontrivial symmetry operation, whereas in the latter one we have only a trivial symmetry operation, i.e., identity.

A. Phenomenology and the microscopic model of the ratchet current

At normal light incidence, the C_s symmetry allows for the following relations between the photocurrent density $\boldsymbol{j}$, magnetization $\boldsymbol{M}$, and radiation Stokes parameters:

$$\begin{aligned} j_x &= \Xi(\chi_1 P_{\rm lin} + \chi_0) + M_z \Xi(\Phi_1 P'_{\rm lin} + \gamma P_{\rm circ}), \\ j_y &= \Xi(-\tilde{\chi}_1 P'_{\rm lin} + \tilde{\gamma} P_{\rm circ}) + M_z \Xi(\tilde{\Phi}_1 P_{\rm lin} + \Phi_0), \end{aligned} \tag{21}$$

where Ξ is proportional to the square of the radiation electric field E_0, and $P_{\rm circ} = i(e_x e_y^* - e_x^* e_y)$ is the circular polarization degree. Comparing with the phenomenological Eqs. (6) obtained for the individual triangles with higher symmetry, we see two differences. First, the linear-polarization sensitive contributions, instead of single coefficients χ and Φ, are now described by independent constants $\tilde{\chi}_1 \neq \chi_1$ and $\tilde{\Phi}_1 \neq \Phi_1$. Second, and crucial, the basically new photocurrent contributions appear, which are the polarization-independent ones described by the constants Φ_0 and χ_0, and the helicity-driven photocurrents given by the constants γ and $\tilde{\gamma}$. In the case when the symmetry is reduced further to C_1, phenomenological equations become lengthy because now j_x as well as j_y are given by a sum of all contributions present in both Eqs. (21) with independent weights. Below, to be specific, we consider for simplicity the microscopic model for the C_s symmetry.

Microscopically, electrons feel the low symmetry of the whole system via the inhomogeneous near-field formed by radiation diffraction from the triangle's boundaries. This near-field $\boldsymbol{E}(\boldsymbol{r})$ has a profile periodic in two-dimensional space with the period of the lateral superlattice; see Fig. 8. Another field acting on electrons is the periodic potential $V(\boldsymbol{r})$ with barriers on the borders of the antidots; see Fig. 8(b). Although both the near-field and the periodic potential are zero on average, the following lateral asymmetry parameter is finite:

$$\Xi = \overline{E_0^2(\boldsymbol{r}) \nabla_x V(\boldsymbol{r})}, \tag{22}$$

where the line denotes averaging over the structure period. The parameter Ξ, already introduced in the phenomenological Eqs. (21), reflects the C_s symmetry of the system giving rise to the corresponding photocurrent contributions. It is clear that $\Xi = 0$ if both the profile of $V(\boldsymbol{r})$ and $E_0^2(\boldsymbol{r})$ have identical coordinate dependence. However, the near-field profile is different from that of the triangles, see Fig. 8(b), and subsequently the parameter Ξ is nonzero. Note that in the case of C_1 point group, an additional lateral asymmetry parameter $\overline{E_0^2(\boldsymbol{r}) \nabla_y V(\boldsymbol{r})}$ emerges.

While in metamaterials with $\lambda \gg d$ the microscopic mechanism of the polarization-dependent photocurrent contributions proportional to $P_{\rm lin}$ and $P'_{\rm lin}$ is similar to that obtained above for the isolated triangle antidots, the polarization-independent one is new. Below we develop the theory of ratchet effects yielding these contributions. We show that they are caused by a radiation-induced electron gas heating, which results in a coordinate-dependent temperature increase, see $\delta T(\boldsymbol{r})$ in Fig. 8(b), which follows the spatially dependent electric field squared $|\boldsymbol{E}(\boldsymbol{r})|^2$ formed due to the near-field of diffraction of THz radiation.

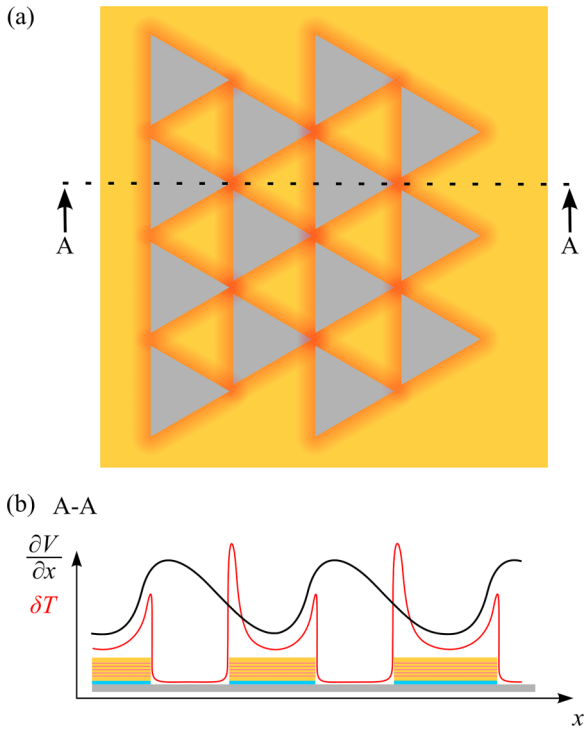

FIG. 8. Model for the Seebeck ratchet current. Panel (a) depicts the ensemble of equilateral-triangle shaped antidots arranged in a slightly distorted hexagonal lattice having C_s-symmetry and the electron temperature profile due to heating of the near-field, schematically highlighted by the red contour. Panel (b) shows the temperature profile $\delta T(\boldsymbol{r}) \propto E_0^2(\boldsymbol{r})$ caused by radiation near-field diffraction at the edges of antidots and the electrostatic force proportional to $\partial V/\partial x$. The figure shows that both terms are asymmetric due to the triangular shape of the antidots.

B. Seebeck ratchet current at M = 0

We begin with the Seebeck ratchet photocurrent formed at zero magnetization. As addressed above, the model of its generation is based on electron gas heating by the near-field $\boldsymbol{E}(\boldsymbol{r})$. The heating results in the emergence of an inhomogeneous profile of electron temperature $\delta T(\boldsymbol{r}) \propto |\boldsymbol{E}(\boldsymbol{r})|^2$. It is found from the energy balance:

$$N\frac{k_{\rm B}\delta T(\boldsymbol{r})}{\tau_T} = \frac{2\sigma_0}{1+(\omega\tau_1)^2}|\boldsymbol{E}(\boldsymbol{r})|^2, \tag{23}$$

where $k_{\rm B}$ is the Boltzmann constant, τ_T is the temperature relaxation time, σ_0 is the dc conductivity, and τ_1 taken at the Fermi energy is the transport relaxation time. This inhomogeneous heating leads to a spatial modulation of the dc conductivity $\delta\sigma(\boldsymbol{r}) = \delta T(\boldsymbol{r})\partial\sigma_0/\partial T$ provided by the temperature dependence $\sigma_0(T)$. As a result, the acceleration of electrons by the periodic electric field $(-1/e)\nabla V(\boldsymbol{r})$ is decompensated, and the electric current is generated with the density [11]

$$j_x = -\frac{1}{2e}\frac{\partial\sigma_0}{\partial T}\overline{\delta T(\boldsymbol{r})\nabla_x V(\boldsymbol{r})}. \tag{24}$$

As the near-field profiles, formed at the borders of neighboring antidots, overlap, we obtain different electric field amplitudes. Consequently, temperatures differ at the triangle bases and apexes along the x-axis; see Fig. 8(b). This figure also demonstrates that the electrostatic force proportional to $\partial V/\partial x$ along this axis, being caused by the triangular shape of the antidots, is asymmetric as well. Therefore, the above average is nonzero giving rise to the Seebeck ratchet current, which is described by the constant χ_0 in Eqs. (21),

$$j_x = \Xi\chi_0 = -\Xi\frac{\sigma_0\tau_T\partial\sigma_0/\partial T}{eNk_{\rm B}\left(1+\omega^2\tau_1^2\right)}. \tag{25}$$

Note that there is an additional contribution to the photocurrent not related to electron heating. It is caused by the dynamic carrier-density redistribution (DCDR) [5,11,48]. This mechanism yields a ratchet current density in the form [48]

$$j_\alpha^{\rm DCDR} = \frac{i}{2e\omega}\Xi\sum_{\beta,\eta=x,y}\frac{\partial\sigma_{\alpha\beta}}{\partial N}\frac{\partial\sigma_{x\eta}(\omega)}{\partial\varepsilon_{\rm F}}e_\eta e_\beta^* + \text{c.c.}, \tag{26}$$

where $\hat{\sigma}$ and $\hat{\sigma}(\omega)$ are the tensors of the dc and ac conductivity. Note that the quantitative estimation of the Seebeck ratchet current requires knowledge of the parameter Ξ, which is defined by the values of the electrostatic potential gradient and the near-field effect induced $E_0^2(\boldsymbol{r})$ being unknown for our structures so far.

C. Spin ratchet current caused by the magnetization

Now we turn to the magnetization-induced ratchet effect. Similarly to the Seebeck contribution considered above, the photocurrent $j_y = M_z\Phi_0\Xi$ microscopically also appears due to inhomogeneous heating of the electron gas resulting in the spatially oscillating temperature correction profile $\delta T(\boldsymbol{r})$. We refer to this contribution as the anomalous Nernst ratchet current.

In the presence of magnetization, the electron dc conductivity is a tensor with the off-diagonal conductivity component σ_{yx}. It is odd in M_z and $\sigma_{yx} \propto M_z$ at low magnetization. The presence of the Hall conductivity is crucial for the magnetization-induced polarization-independent contribution. In the presence of magnetization, the static periodic force of the potential $V(\boldsymbol{r})$ results in the perpendicular electric current component $j_y(\boldsymbol{r}) = (-1/e)\sigma_{yx}\nabla_x V(\boldsymbol{r})$. Due to the radiation near-field, a spatially oscillating part of the Hall conductivity $\delta\sigma_{yx}(\boldsymbol{r}) = \delta T(\boldsymbol{r})\partial\sigma_{yx}/\partial T$ emerges that is odd in M_z. As a result, we obtain the anomalous Nernst ratchet current in the form

$$j_y(M_z) = -\frac{1}{e}\frac{\partial\sigma_{yx}}{\partial T}\overline{\delta T(\boldsymbol{r})\nabla_x V(\boldsymbol{r})}. \tag{27}$$

The corresponding term in Eq. (21) is given by

$$j_y = M_z\Xi\Phi_0 = -\Xi\frac{2\sigma_0\tau_T\partial\sigma_{yx}/\partial T}{eNk_{\rm B}\left(1+\omega^2\tau_1^2\right)}. \tag{28}$$

Like the zero-magnetization polarization-independent ratchet current, there is also a magnetization-dependent contribution to the photocurrent caused by the DCDR mechanism and not related to electron heating. Due to the AHE, we have the off-diagonal conductivity component $\sigma_{yx} \propto M_z$. Taking for unpolarized radiation in Eq. (26) $e_\eta e_\beta^* = \delta_{\eta\beta}/2$, and the ac conductivity in the form $\sigma_{xx}(\omega) = \sigma_0/(1-i\omega\tau_1)$, with σ_0

being linear in the Fermi energy, we obtain the following polarization-independent spin ratchet current density:

$$j_y^{\mathrm{DCDR}} = -\Xi \frac{\sigma_0 \tau_1 \partial \sigma_{yx}/\partial N}{2e\varepsilon_{\mathrm{F}}\left(1+\omega^2\tau_1^2\right)}. \tag{29}$$

This expression shows that the DCDR mechanism is based on the electron concentration dependence of the AHE conductivity rather than on its dependence on temperature.

VI. DISCUSSION

A. Seebeck spin ratchet

The THz radiation-driven Seebeck ratchet and spin ratchet effects considered above manifest themselves in the presence of the polarization-independent photocurrents $J_{\mathrm{R}}^{\mathrm{nm}}$ and $J_{\mathrm{R}}^{\mathrm{m}}$, respectively. They are clearly detected in experiments applying radiation with $\lambda = 118\,\mu\mathrm{m}$, see Figs. 2(a) and 3, but absent in results obtained with two orders of magnitude smaller wavelength $\lambda = 0.8\,\mu\mathrm{m}$. This observation is an important consequence of the symmetry reduction from trigonal C_{3v}-symmetry to the lower one (Sec. V) and is fully in line with the phenomenological Eqs. (6) and (21) obtained for the individual triangles with symmetry C_{3v} (probed at $\lambda \leqslant d$) and metamaterial with symmetry C_s or C_1 (probed at $\lambda \gg d$), respectively. The reduction of symmetry may be caused by different factors such as deviation of the antidot positions in the superlattice, nonideal and different shapes of the triangles, as well as by the fact that the lateral structure is smaller than the beam spot, and consequently this structure cannot be considered as infinite. Equations (6) and (21) show that while the polarization dependence of the photocurrents in both cases is defined by the Stokes parameters P_{lin} and P'_{lin}, the polarization-independent contributions are present only in the case $\lambda \gg d$ and forbidden for the photoexcitation of the individual triangles realized for $\lambda \leqslant d$.

For the C_s-symmetry describing an infinite superlattice, the zero-magnetization contribution $J_{\mathrm{R}}^{\mathrm{nm}}$ becomes possible in the x-direction, i.e., along the height of the triangles. This photocurrent was indeed observed in the experiment; see the red trace in Fig. 2(a). The microscopic derivation of the polarization-independent photocurrent density j_x presented in Sec. V, which is obtained for the C_s symmetry, gives an intuitive picture. Indeed, the spatial temperature profile due to the near-field-induced heating is insensitive to the electric field orientation; see Eq. (23). The corresponding asymmetric profile of the temperature $\delta T(x)$ together with the asymmetric electrostatic force $\partial V/\partial x$, see Fig. 8(b), yields a polarization-independent Seebeck ratchet current in the x-direction. Note that without magnetization the spin of electrons is not involved in the photocurrent formation. In the experiment, we also detected a polarization-independent photocurrent in the y-direction; see the blue trace in Fig. 2(a). This observation indicates a further symmetry reduction from C_s with a reflection plane (xz) to C_1 which has no nontrivial symmetry operations.

The magnetization induced in the layers because of the magnetic field applied in the z-direction results—in agreement with the theoretical consideration—in photocurrents proportional to M_z: they exhibit a hysteresis at small magnetic fields, become constant at high magnetic fields, and change sign at reversal of the magnetization M_z. Note that, also in line with theory, the magnetic-field even parts do not change upon variation of the magnetic field; see the insets in Fig. 4. Comparing the hysteresis traces of the spin ratchet current $J_{\mathrm{R}}^{\mathrm{m}}$ with the Faraday rotation angle, measured in the unpatterned Co/Pt multilayer film, shows that both have equal widths; see Fig. 5. This demonstrates that the $J_{\mathrm{R}}^{\mathrm{m}}$ photocurrent is formed in the bulk of the material, which is in agreement with the mechanism of the spin ratchet current originating from the spatially periodic temperature gradient caused by the near-field of diffraction; see Sec. V A and Fig. 8. The spin ratchet is caused by the AHE; see Sec. V C. It is generated in the direction normal to the Seebeck ratchet effect. For C_s symmetry the latter one is given by $j_x = \Xi\chi_0$ [see Eqs. (21), (24), and (25)] and the spin ratchet is described by $M_z\Xi\Phi_0$; see Eqs. (21), (27), and (28). Note that in both zero-magnetization and the spin ratchet effect, a photocurrent due to the dynamic carrier-density redistribution can yield additional contributions; see Eqs. (26) and (29). Both mechanisms behave equally upon variation of polarization, lateral asymmetry parameter Ξ, and frequency. Therefore, experimental discrimination between them is a challenging task and beyond the scope of the present paper.

B. Trigonal spin photocurrent

Now we consider the polarization-dependent photoresponse. Figures 2 and 3 reveal that the photocurrent exhibits a characteristic dependence on the orientation of the radiation electric field vector relative to the bases of the triangle antidots. Figure 2 shows that the photocurrent contributions excited in the x- and y-directions for both $\lambda \approx d$ and $\lambda \gg d$ vary, respectively, as P_{lin} and P'_{lin}, which are given by Eq. (8). This observation is fully in line with the phenomenological theory obtained for the isolated triangles [see Eqs. (6)] as well as for the metamaterial [see Eqs. (21)]. The microscopic mechanism of the zero-magnetization polarization-dependent photocurrent contributions is described in Sec. IV B. It is based on asymmetric scattering on the triangle antidot boundaries and yields a spin-independent photocurrent. As expected, this mechanism also yields the polarization dependence observed in the experiment. For $\lambda \approx d$, the amplitudes of the photocurrents j_x and j_y are defined by the same parameter χ given by Eq. (12). Equal amplitudes for both photocurrents are indeed observed in experiments with $\lambda = 0.8\,\mu\mathrm{m}$; see Fig. 2(b). For $\lambda \gg d$, the corresponding parameters χ_1 and $\tilde{\chi}_1$ become independent, i.e., they may have different values. In the corresponding experiment with $\lambda = 118\,\mu\mathrm{m}$ they differ, however, only slightly (by about a factor 1.4); see Fig. 2(a) [84]. This observation shows that also in this case the microscopic origin of the photocurrent can be well described by the mechanism introduced in Sec. IV B, which considers C_{3v} symmetry and yields equal factors for j_x and j_y. Microscopically, it stems from the asymmetric scattering at the antidots boundaries; see Figs. 7(a) and 7(b).

The magnetization M_z results in a phase shift of the polarization-dependent contributions; see Fig. 3(a). It is caused by the emergence of the magnetization-induced photocurrent, which is 45° phase-shifted with respect to the zero-magnetization one; see Eqs. (21). The experimental

traces for $J_x^{\rm nm}$ and $J_x^{\rm m}$ in Fig. 3(b) are in full agreement with the phenomenological Eqs. (21) and (8) as well as with the microscopic theory of the trigonal photocurrents presented in Sec. IV. Like the spin ratchet, the magnetization-driven trigonal photocurrent $J_{\rm tr}^{\rm m}$ exhibits an hysteresis at small magnetic fields, becomes constant at high fields, and changes its sign switching the sign of M_z; see Figs. 4(b) and 5(b). Microscopically, the trigonal photocurrent proportional to M_z is caused by skew scattering (see Secs. IV C 1 and IV C 2) and magnetization-dependent scattering; see Sec. IV C 3.

While the above mechanisms are considered theoretically, we note that an additional microscopic mechanism may give rise to the polarization-dependent photocurrent. One could explain it by the polarization-dependent lateral anisotropy of the laser heating, which leads to the anomalous Nernst effect. The anisotropy may be obtained considering the patterned structure as a near-field antenna, which results in the laser heating around small central regions, i.e., increased temperature in the vicinity of the triangle's vertices. This yields a maximum of the radiation absorption, when the light polarization is parallel to the heights of triangles, and it creates the polarization-dependent temperature gradients $\nabla T(\alpha)$ with triangular space symmetry. Due to the magnetization, this spatial temperature profile results in the trigonal ANE current $\boldsymbol{j}^{\rm ANE} \propto \boldsymbol{M}\times\nabla T$. This contribution also has a $j_x^{\rm ANE} \propto \sin 2\alpha$ dependence on the polarization orientation as the current $J_{\rm tr}^{\rm m}$ detected in the experiment; Fig. 3(b). A theoretical treatment of this mechanism is a task for future research. Note that in the above mechanism, as well as in the mechanisms considered theoretically in Secs. IV C 1 and IV C 2, the photocurrent $J_{\rm tr}^{\rm m}$ is spin-polarized and can be classified as a trigonal spin current. The quantitative estimation of the temperature-gradient-driven photocurrent requires knowledge of the antenna coupling magnitude, which is absent so far.

Finally, we discuss the hysteresis width of the trigonal spin current $J_{\rm tr}^{\rm m}$. Surprisingly, it is about two times larger than that of the spin ratchet current, as well as of the hysteresis of the Faraday rotation angle in the unpatterned Co/Pt films; see photocurrent traces (red and blue lines) and Faraday angle traces (gray lines) in Figs. 5(a) and 5(b). We emphasize that both photocurrent traces were obtained from one experiment and were extracted using the difference in the polarization dependence. Different hysteresis widths for the spin ratchet and trigonal contributions are clearly seen in the original data sets obtained for different azimuth angles α (see Fig. 12), particularly for $\alpha = 135^\circ$ at which $J_{\rm R}^{\rm m}$ and $J_{\rm tr}^{\rm m}$ have opposite signs. This difference clearly indicates that the trigonal photocurrent and the spin ratchet current are formed in different regions of the superlattice. This is in line with the microscopic theory developed above. We have shown that the trigonal photocurrent is formed at the boundaries of the triangle antidots, see Sec. IV, whereas the spin ratchet current is generated in the film bulk; see Sec. V C. While our paper is primarily aimed at the spin ratchet, the larger hysteresis width of the trigonal photocurrent needs an additional discussion. As we addressed above, the hysteresis width of the spin ratchet current coincides with that of the magnetization measured by Faraday rotation in the unpatterned films, which agrees with the theory developed in Sec. V C. The deviation of the hysteresis width in the trigonal current with respect to the magnetization in the homogeneous film should be caused by the difference between the magnetization of the unpatterned film and the film in the vicinity of the antidot boundaries. This can be caused by the enhanced electric fields due to the near-field of diffraction and, related to local heating, inhomogeneity of M_z at the antidot edges, magnetic domain formation in the superlattice, domain wall pinning, etc. Additional experiments using a pulsed laser operating at a similar frequency but almost five orders of magnitude higher intensity demonstrated that such a drastic increase in the radiation electric field scales only the signal magnitude but does not change the hysteresis widths of $J_{\rm tr}^{\rm m}$; see Fig. 6. This result excludes changes in the magnetization behavior induced by the radiation electric field, e.g., due to the heating of the antidot edges. Note that this is not surprising, because in both cases one would expect a narrowing of the magnetization hysteresis.

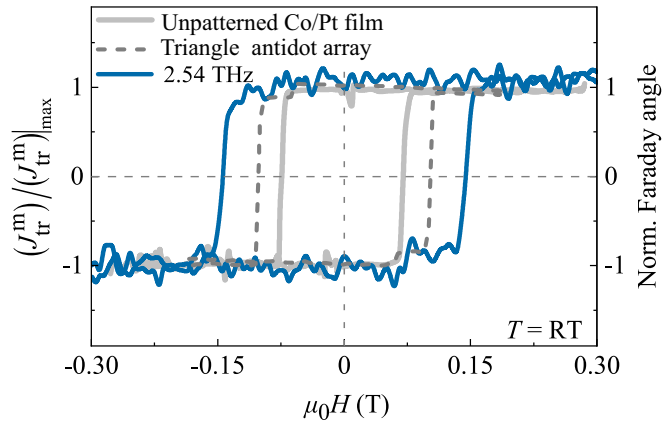

FIG. 9. Magnetic field dependence of the magnetization-induced polarization-dependent photocurrent contribution (blue curve) and Faraday angles measured in unpatterned Co/Pt film (solid curve) and the array of the equilateral triangle-shaped antidots (dashed curve). The photocurrent is measured in the x-direction and normalized on its maximum, $(J_{\rm tr}^{\rm m})/(J_{\rm tr}^{\rm m})|_{\rm max}$. Faraday angle traces are also normalized on their maximum values. Coercive fields obtained from the Faraday angle traces are larger for the antidots array ($\mu_0 H_{\rm c} = 102$ mT) than that for the unpatterned Co/Pt film with the same layer design (76 mT). Note that Faraday rotation yields the integrated response from the whole structure. The coercive field for the trigonal photocurrent is $\mu_0 H_{\rm c} = 144$ mT. The photocurrent is formed because of scattering at the triangle boundaries. Consequently, it probes the local magnetization in the vicinity of the antidot edges.

Performing additional experiments on Faraday rotation on unpatterned films and patterned films with the lateral antidot superlattice, we observed that the hysteresis width in the latter case is larger than in the former one; see Fig. 9. Note that in the magneto-optic experiments, we obtain the integrated response from the bulk part and the antidot edges, whereas the trigonal photocurrent gives a signal proportional to the magnetization at the edges only. This result suggests that the larger hysteresis width detected in $J_{\rm tr}^{\rm m}$ is most probably related to spatially inhomogeneous switching of the magnetization M_z. We can give three simple reasons that may explain the increased width of the magnetic hysteresis in the patterned region. First, we expect that magnetization reversal in perpendicularly magnetized Co/Pt films proceeds via domain-wall nucleation and

propagation. Due to the stray field of the perpendicularly magnetized films, the nucleation field is reduced. However, since at the edges of the triangles the magnetic film has been removed, the stray field is diminished in the edge regions leading to an increased nucleation/switching field. Second, domain walls are pinned at the apexes of triangles so as to reduce the wall area. Third, in the region of the edges, defects and pinning sites introduced by lithographic structuring may hinder the propagation of domain walls which are nucleated in the center of the elements towards the edges, leading again to a locally increased switching field.

Summarizing, all theoretical functional dependences are clearly reproduced in the experiment: The dependences of the photocurrent on the polarization azimuthal angle given by theoretical Eqs. (6)–(8) and (21) are shown by solid lines in Figs. 2 and 3, which perfectly fit the experimental data on both magnetization-dependent and -independent photocurrents. Then, the hysteretic behavior of the polarization-independent magnetization-dependent photocurrent in magnetic field given by Eqs. (27)–(29) is clearly seen in Figs. 4–6 and 9 as well as Figs. 12 and 13.

VII. SUMMARY

Our results demonstrate that terahertz radiation with a wavelength substantially larger than the period of the array of the triangle-shaped antidots fabricated from Co/Pt films results in a polarization-independent current shown to be caused by the anomalous Nernst spin ratchet effect. It is generated in the film bulk and exhibits hysteresis in a magnetic field range comparable to that of the Faraday rotation data measured in unpatterned samples. The developed theory reveals that the current is caused by the temperature gradient generated by the near-field of diffraction and, in the presence of magnetization, is due to spin-dependent scattering resulting in the spin-polarized current. The polarization-dependent trigonal spin photocurrent, also detected in our experiments, is generated by both terahertz and infrared radiation. It is formed at individual triangles, and in the presence of magnetization it is generated due to spin- and magnetization-dependent electron scattering. The trigonal spin photocurrent has a larger hysteresis width than that of the Nernst spin ratchet current because of the spatial inhomogeneity of the magnetization probed by the polarization-dependent photocurrent generated in the region of the antidot edges. This observation enables us to study the magnetization at the metal film's edges.

ACKNOWLEDGMENTS

We thank C. Gorini for the fruitful discussions. The support of the Deutsche Forschungsgemeinschaft (DFG, German Research Foundation) Project No. Ga501/18, IRAP Programme of the Foundation for Polish Science (Grant No. MAB/2018/9, project CENTERA), the Volkswagen Stiftung Program (97738), JSPS KAKENHI (Grants No. 21H04649 and No. 22K18962), the Research Foundation for Opto-Science and Technology, the Asahi Glass Foundation, the Support Center for Advanced Telecommunications Technology Research Foundation, and the Tanaka Memorial Foundation is gratefully acknowledged. Sample fabrication was supported by Nanotechnology Platform Program of the Ministry of Education, Culture, Sports, Science and Technology (MEXT), Japan, Grant No. JPMXP09-F21-NU-0046, Nagoya University.

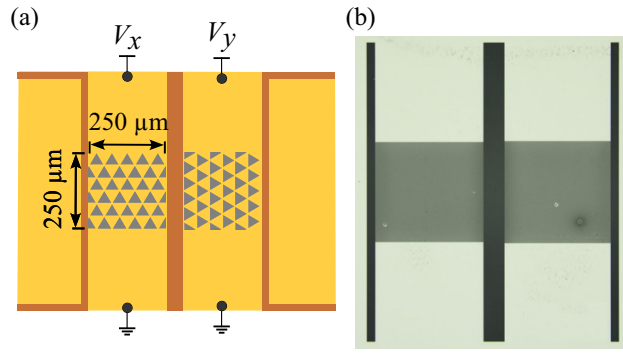

FIG. 10. Sketch of the studied sample consisting of two electrically isolated arrays of the triangle-shaped antidots rotated by 90° with respect to each other. The arrays have a size of 250×250 µm^2 and a period of 0.55 µm. Note that the triangles in the sketch are oversized for better visibility. Two pairs of contacts allow one to probe the photocurrent along the height (left part) and the basis (right side) of the triangles, i.e., in the x- and y-direction.

APPENDIX A: SAMPLE CHARACTERISTICS

The investigated sample hosts two lateral superlattices formed by the triangle-shaped antidots, which are rotated by 90° with respect to each other; see Fig. 10. The arrays are electrically isolated using electron beam lithography and laser cutting (see Ref. [51] for more details). This allowed us to probe the photocurrent in the x- and y-directions simultaneously in a single experiment.

Figure 11(a) shows the magnetic field of the dark resistance of the metamaterial measured in a two-point configuration with a bias current of 100 nA. It shows that in the studied magnetic field range from −2 to 2 T, the resistance remains unchanged. It also exhibits only a weak dependence on temperature; see Fig. 11(b).

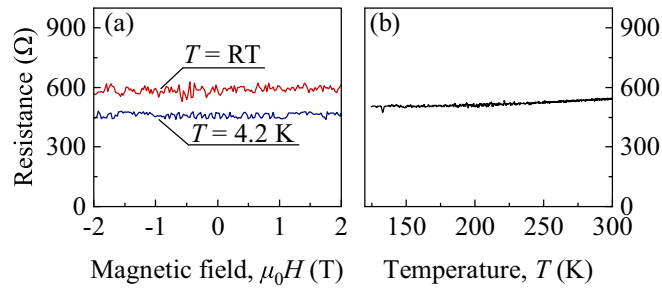

FIG. 11. (a) Dark resistance as a function of magnetic field measured along the triangles' height with a two-point measurement setup. (b) Temperature dependence of the dark resistance at $\mu_0 H = 0$.

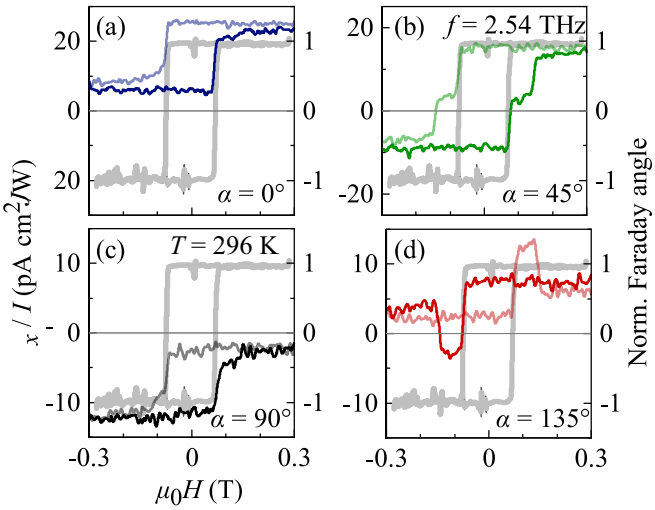

FIG. 12. The angle has been chosen such that in the formula $A_1 \cos 2\alpha + C_1 + M_z A_2 \sin 2\alpha + MC_2$ either the sine or cosine function vanishes and the remaining part changes its sign by adding 90° [compare panel (a) with (c) and (b) with (d)]. The dashed lines indicate the magnetization-independent contribution $A_1 \cos 2\alpha + C_1$, which reduces to C_1 for 45° and 90°. Curves with full and reduced opacity show the forward and backward magnetic field sweeps, respectively. The gray lines show the magnetic field dependence of the Faraday rotation angle obtained in the unpatterned Co/Pt film normalized on its maximum value.

APPENDIX B: HYSTERESIS OF THE TRIGONAL PHOTOCURRENT MEASURED FOR DIFFERENT AZIMUTH ANGLES

Figure 12 shows the hysteresis of the photocurrent measured for four different azimuth angles α. The angles are selected in such a way that the polarization-dependent contribution $J_x = M_z A_2 \sin 2\alpha$ either vanishes and only the polarization-independent part forms the photocurrent ($\alpha = 0, 90°$), or it has a maximum and opposite signs at $\alpha = 45°, 135°$. The figure reveals that in the former case, the hysteresis width coincides with the magneto-optical Faraday data of the unpatterned Co/Pt multilayer film (gray traces). For a radiation electric field applied at angles $\alpha = 45°, 135°$, two different hysteresis widths are clearly seen, leading to a steplike change of the widths. It is particularly pronounced for $\alpha = 135°$ at which the polarization-dependent and polarization-independent parts have opposite signs.

APPENDIX C: SQUID AND MAGNETO-OPTIC KERR MICROSCOPY DATA

To study the magnetization switching properties of the sample in the patterned and unpatterned regions, we performed additional experiments.

Superconducting quantum interference device (SQUID) measurements are used to determine the magnetic properties of the full sample. In Fig. 13 we show the SQUID data obtained in a sample with the same design. In Fig. 13(a) a SQUID loop measured with magnetic field applied perpendicular to the sample plane and ranging from +4 to −1.5 T is shown. The measurements reveal magnetization saturation

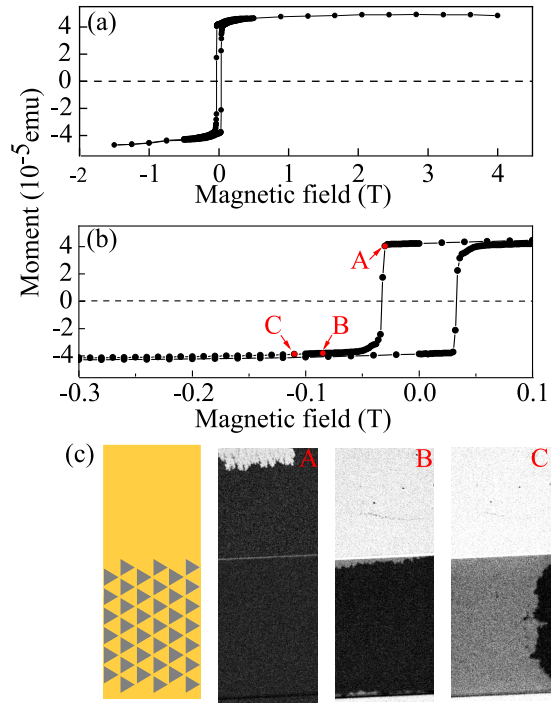

FIG. 13. (a),(b) SQUID loop measured on the full film sample with unpatterned (plane Co/Pt film) and patterned (array of triangular antidots) regions; see the sketch shown on the left side of panel (c). The loops are measured for magnetic fields in a range from −1.5 to 4 T applied perpendicular to the sample plane; see panel (a). Panel (b) is a zoom-in showing the data for magnetic fields varying from −0.3 to 0.1 T. Panel (c) shows the sample sketch (left) and the Kerr microscopy images taken at the points marked in panel (a) for magnetic fields: −30 mT [point A in panel (b)]; −84 mT (point B); and −110 mT (point C). In (c) black and white contrast corresponds to upward and downward out-of-plane magnetization, respectively.

at around 1.5 T and a coercive field of around 33 mT, as can be seen in the zoom-in in Fig. 13(b). Figure 13(c) shows polar Kerr-microscopy images in which both patterned and unpatterned parts of the sample were captured simultaneously. The images show the magnetization state during the reversal process (black and white corresponds to upward and downward out-of-plane magnetization, respectively) after application of magnetic fields with different amplitudes. The unpatterned region of the sample shows a coercivity of around 33 mT. Interestingly, to switch the magnetization in the patterned part of the sample, a much larger magnetic field needs to be applied, as can be seen in the lower parts of the Kerr-microscopy images. In the measured SQUID loop, a large jump in the signal is observed when the unpatterned part of the magnetic film switches since most of the sample is unpatterned and SQUID is an integrating measurement technique. Note that the spatial resolution of the Kerr microscope does not allow the detection of magnetization reversal of the individual triangles, however their influence as pinning centers for magnetization reversal can nevertheless be detected.

Magnetization reversal processes in thin films are strongly influenced by crystal defects in the ferromagnetic layer leading to nucleation and pinning sites for domain walls. This is true for both the patterned and the unpatterned part of the

sample (see, e.g., the fringed domain wall in the upper part of the first image taken at −30 mT). Since a single triangle can be subdivided into an inner part untouched by the structuring process and the rim of the triangle, in which crystal defects are very likely to have been introduced by the mechanical treatment during the structuring process, the magnetization reversal of a single perpendicularly magnetized triangle could be stepwise. At lower magnetic fields, the inner part of the triangle switches by domain nucleation and propagation since the typical domain wall width for Co/Pt multilayer is much smaller than the size of a triangle. However, the switching process at the rim of a triangle differs for three reasons. First, the missing material reduces the amount of stray field, which aids magnetization switching in perpendicularly magnetized materials, and second, domain walls are pinned at the apexes of triangles so as to reduce the wall area. Third, domain-wall propagation towards the rim of the triangles may be hindered by defects and pinned moments. This would also be in line with the SQUID data, which show saturation of a fraction of the magnetization only at very large magnetic fields.

[1] F. Jülicher, A. Ajdari, and J. Prost, Rev. Mod. Phys. **69**, 1269 (1997).
[2] H. Linke, Appl. Phys. A **75**, 167 (2002).
[3] P. Reimann, Phys. Rep. **361**, 57 (2002).
[4] P. Hänggi and F. Marchesoni, Rev. Mod. Phys. **81**, 387 (2009).
[5] E. L. Ivchenko and S. D. Ganichev, JETP Lett. **93**, 673 (2011) [Pis'ma Zh. Eksp. Teor. Fiz. **93**, 752 (2011)].
[6] G. V. Budkin, L. E. Golub, E. L. Ivchenko, and S. D. Ganichev, JETP Lett. **104**, 649 (2016).
[7] B. Lau and O. Kedem, J. Chem. Phys. **152**, 200901 (2020).
[8] P. Olbrich, J. Allerdings, V. V. Bel'kov, S. A. Tarasenko, D. Schuh, W. Wegscheider, T. Korn, C. Schüller, D. Weiss, and S. D. Ganichev, Phys. Rev. B **79**, 245329 (2009).
[9] E. S. Kannan, I. Bisotto, J.-C. Portal, R. Murali, and T. J. Beck, Appl. Phys. Lett. **98**, 193505 (2011).
[10] P. Olbrich, J. Karch, E. L. Ivchenko, J. Kamann, B. März, M. Fehrenbacher, D. Weiss, and S. D. Ganichev, Phys. Rev. B **83**, 165320 (2011).
[11] A. V. Nalitov, L. E. Golub, and E. L. Ivchenko, Phys. Rev. B **86**, 115301 (2012).
[12] T. Otsuji, T. Watanabe, S. A. B. Tombet, A. Satou, W. M. Knap, V. V. Popov, M. Ryzhii, and V. Ryzhii, IEEE Trans. Terahertz Sci. Technol. **3**, 63 (2013).
[13] C. Drexler, S. A. Tarasenko, P. Olbrich, J. Karch, M. Hirmer, F. Müller, M. Gmitra, J. Fabian, R. Yakimova, S. Lara-Avila, S. Kubatkin, M. Wang, R. Vajtai, P. M. Ajayan, J. Kono, and S. D. Ganichev, Nat. Nanotechnol. **8**, 104 (2013).
[14] Y. Kurita, G. Ducournau, D. Coquillat, A. Satou, K. Kobayashi, S. B. Tombet, Y. M. Meziani, V. V. Popov, W. Knap, T. Suemitsu, and T. Otsuji, Appl. Phys. Lett. **104**, 251114 (2014).
[15] G. V. Budkin and L. E. Golub, Phys. Rev. B **90**, 125316 (2014).
[16] P. Faltermeier, P. Olbrich, W. Probst, L. Schell, T. Watanabe, S. A. Boubanga-Tombet, T. Otsuji, and S. D. Ganichev, J. Appl. Phys. **118**, 084301 (2015).
[17] P. Olbrich, J. Kamann, M. König, J. Munzert, L. Tutsch, J. Eroms, D. Weiss, M.-H. Liu, L. E. Golub, E. L. Ivchenko, V. V. Popov, D. V. Fateev, K. V. Mashinsky, F. Fromm, T. Seyller, and S. D. Ganichev, Phys. Rev. B **93**, 075422 (2016).
[18] V. V. Popov, Appl. Phys. Lett. **108**, 261104 (2016).
[19] D. V. Fateev, K. V. Mashinsky, J. D. Sun, and V. V. Popov, Solid-State Electron. **157**, 20 (2019).
[20] S. Hubmann, V. V. Bel'kov, L. E. Golub, V. Y. Kachorovskii, M. Drienovsky, J. Eroms, D. Weiss, and S. D. Ganichev, Phys. Rev. Res. **2**, 033186 (2020).
[21] S. Boubanga-Tombet, W. Knap, D. Yadav, A. Satou, D. B. But, V. V. Popov, I. V. Gorbenko, V. Kachorovskii, and T. Otsuji, Phys. Rev. X **10**, 031004 (2020).
[22] J. A. Delgado-Notario, V. Clericò, E. Diez, J. E. Velázquez-Pérez, T. Taniguchi, K. Watanabe, T. Otsuji, and Y. M. Meziani, APL Photon. **5**, 066102 (2020).
[23] E. Mönch, S. O. Potashin, K. Lindner, I. Yahniuk, L. E. Golub, V. Y. Kachorovskii, V. V. Bel'kov, R. Huber, K. Watanabe, T. Taniguchi, J. Eroms, D. Weiss, and S. D. Ganichev, Phys. Rev. B **105**, 045404 (2022).
[24] K. Tamura, C. Tang, D. Ogiura, K. Suwa, H. Fukidome, Y. Takida, H. Minamide, T. Suemitsu, T. Otsuji, and A. Satou, APL Photon. **7**, 126101 (2022).
[25] E. Mönch, S. O. Potashin, K. Lindner, I. Yahniuk, L. E. Golub, V. Y. Kachorovskii, V. V. Bel'kov, R. Huber, K. Watanabe, T. Taniguchi, J. Eroms, D. Weiss, and S. D. Ganichev, Phys. Rev. B **107**, 115408 (2023).
[26] M. Scheid, M. Wimmer, D. Bercioux, and K. Richter, Phys. Status Solidi C **3**, 4235 (2006).
[27] M. V. Costache and S. O. Valenzuela, Science **330**, 1645 (2010).
[28] M. E. Flatté, Nat. Phys. **4**, 587 (2008).
[29] V. Y. Demikhovskii and D. V. Khomitsky, J. Exp. Theor. Phys. Lett. **83**, 340 (2006).
[30] J. Matsuno, T. Lottermoser, T. Arima, M. Kawasaki, and Y. Tokura, Phys. Rev. B **75**, 180403(R) (2007).
[31] M. Scheid, A. Pfund, D. Bercioux, and K. Richter, Phys. Rev. B **76**, 195303 (2007).
[32] B. Braunecker, D. E. Feldman, and F. Li, Phys. Rev. B **76**, 085119 (2007).
[33] C.-H. Lin, C.-S. Tang, and Y.-C. Chang, Phys. Rev. B **78**, 245312 (2008).
[34] S. Smirnov, D. Bercioux, M. Grifoni, and K. Richter, Phys. Rev. Lett. **100**, 230601 (2008).
[35] F. Liang, Y. H. Yang, and J. Wang, Eur. Phys. J. B **69**, 337 (2009).
[36] S. Smirnov, D. Bercioux, M. Grifoni, and K. Richter, Phys. Rev. B **80**, 201310(R) (2009).
[37] M. Scheid, D. Bercioux, and K. Richter, Chem. Phys. **375**, 276 (2010).
[38] J.-D. Lu, Microelectron. Eng. **87**, 216 (2010).
[39] R. M. Abdullah, A. J. Vick, B. A. Murphy, and A. Hirohata, J. Phys. D **47**, 482001 (2014).
[40] Y. S. Ang, Z. Ma, and C. Zhang, Sci. Rep. **5**, 7872 (2015).
[41] O. Gomonay, M. Kläui, and J. Sinova, Appl. Phys. Lett. **109**, 142404 (2016).
[42] X. Chen, X. Zhou, R. Cheng, C. Song, J. Zhang, Y. Wu, Y. Ba, H. Li, Y. Sun, Y. You, Y. Zhao, and F. Pan, Nat. Mater. **18**, 931 (2019).
[43] P. R. Zangara, J. Henshaw, D. Pagliero, A. Ajoy, J. A. Reimer, A. Pines, and C. A. Meriles, Nano Lett. **19**, 2389 (2019).

[44] Y.-H. Huang, C.-Y. Yang, C.-W. Cheng, A. Lee, C.-H. Tseng, H. Wu, Q. Pan, X. Che, C.-H. Lai, K.-L. Wang, H.-J. Lin, and Y.-C. Tseng, Adv. Funct. Mater. **32**, 2111653 (2022).

[45] S. Vélez, S. Ruiz-Gómez, J. Schaab, E. Gradauskaite, M. S. Wörnle, P. Welter, B. J. Jacot, C. L. Degen, M. Trassin, M. Fiebig, and P. Gambardella, Nat. Nanotechnol. **17**, 834 (2022).

[46] D. Bercioux and P. Lucignano, Rep. Prog. Phys. **78**, 106001 (2015).

[47] P. Faltermeier, G. V. Budkin, J. Unverzagt, S. Hubmann, A. Pfaller, V. V. Bel'kov, L. E. Golub, E. L. Ivchenko, Z. Adamus, G. Karczewski, T. Wojtowicz, V. V. Popov, D. V. Fateev, D. A. Kozlov, D. Weiss, and S. D. Ganichev, Phys. Rev. B **95**, 155442 (2017).

[48] P. Faltermeier, G. V. Budkin, S. Hubmann, V. V. Bel'kov, L. E. Golub, E. L. Ivchenko, Z. Adamus, G. Karczewski, T. Wojtowicz, D. A. Kozlov, D. Weiss, and S. D. Ganichev, Phys. E **101**, 178 (2018).

[49] P. Sai, S. O. Potashin, M. Szoła, D. Yavorskiy, G. Cywiński, P. Prystawko, J. Łusakowski, S. D. Ganichev, S. Rumyantsev, W. Knap, and V. Y. Kachorovskii, Phys. Rev. B **104**, 045301 (2021).

[50] C. Betthausen, T. Dollinger, H. Saarikoski, V. Kolkovsky, G. Karczewski, T. Wojtowicz, K. Richter, and D. Weiss, Science **337**, 324 (2012).

[51] M. Matsubara, T. Kobayashi, H. Watanabe, Y. Yanase, S. Iwata, and T. Kato, Nat. Commun. **13**, 6708 (2022).

[52] V. V. Bel'kov and S. D. Ganichev, Semicond. Sci. Technol. **23**, 114003 (2008).

[53] A. Lorke, S. Wimmer, B. Jager, J. Kotthaus, W. Wegscheider, and M. Bichler, Phys. B: Condens. Matter **249-251**, 312 (1998).

[54] A. D. Chepelianskii, M. V. Entin, L. I. Magarill, and D. L. Shepelyansky, Eur. Phys. J. B **56**, 323 (2007).

[55] S. Sassine, Y. Krupko, J.-C. Portal, Z. D. Kvon, R. Murali, K. P. Martin, G. Hill, and A. D. Wieck, Phys. Rev. B **78**, 045431 (2008).

[56] E. S. Kannan, I. Bisotto, J.-C. Portal, T. J. Beck, and L. Jalabert, Appl. Phys. Lett. **101**, 143504 (2012).

[57] M. Motta, L. Burger, L. Jiang, J. D. González Acosta, i. c. v. L. Jelić, F. Colauto, W. A. Ortiz, T. H. Johansen, M. V. Milošević, C. Cirillo, C. Attanasio, C. Xue, A. V. Silhanek, and B. Vanderheyden, Phys. Rev. B **103**, 224514 (2021).

[58] Note that the measurements of the photosignal in the x- and y-direction were performed on two samples with identical design and characteristics but different position of the contacts with respect to the triangles' orientation; see Fig. 10.

[59] K.-M. Dantscher, D. A. Kozlov, M. T. Scherr, S. Gebert, J. Bärenfänger, M. V. Durnev, S. A. Tarasenko, V. V. Bel'kov, N. N. Mikhailov, S. A. Dvoretsky, Z. D. Kvon, J. Ziegler, D. Weiss, and S. D. Ganichev, Phys. Rev. B **95**, 201103(R) (2017).

[60] S. D. Ganichev, W. Prettl, and P. G. Huggard, Phys. Rev. Lett. **71**, 3882 (1993).

[61] S. D. Ganichev, I. N. Yassievich, W. Prettl, J. Diener, B. K. Meyer, and K. W. Benz, Phys. Rev. Lett. **75**, 1590 (1995).

[62] S. D. Ganichev, Y. V. Terent'ev, and I. D. Yaroshetskii, Pis'ma Zh. Tekh. Fiz. **11**, 46 (1985) [Sov. Tech. Phys. Lett. **11**, 20 (1989)].

[63] S. N. Danilov, B. Wittmann, P. Olbrich, W. Eder, W. Prettl, L. E. Golub, E. V. Beregulin, Z. D. Kvon, N. N. Mikhailov, S. A. Dvoretsky, V. A. Shalygin, N. Q. Vinh, A. F. G. van der Meer, B. Murdin, and S. D. Ganichev, J. Appl. Phys. **105**, 013106 (2009).

[64] S. D. Ganichev, Phys. B: Condens. Matter **273-274**, 737 (1999).

[65] Note that application of an in-plane magnetic field does not affect the signals in the whole studied range $|\mu_0 H| \leqslant 2T$.

[66] Note that the sample resistance does not depend on magnetic field; see Fig. 11 in Appendix A.

[67] We note that while in the theoretical consideration the current density j is used, in the experiments the electric current J is measured, which is proportional to the current density j.

[68] P. Olbrich, L. E. Golub, T. Herrmann, S. N. Danilov, H. Plank, V. V. Bel'kov, G. Mussler, C. Weyrich, C. M. Schneider, J. Kampmeier, D. Grützmacher, L. Plucinski, M. Eschbach, and S. D. Ganichev, Phys. Rev. Lett. **113**, 096601 (2014).

[69] S. N. Danilov, L. E. Golub, T. Mayer, A. Beer, S. Binder, E. Mönch, J. Minár, M. Kronseder, C. H. Back, D. Bougeard, and S. D. Ganichev, Phys. Rev. Appl. **16**, 064030 (2021).

[70] V. I. Belinicher and B. I. Sturman, Sov. Phys. Usp. **23**, 199 (1980) [Usp. Fiz. Nauk **1980**, 130 (1980)].

[71] W. Weber, L. E. Golub, S. N. Danilov, J. Karch, C. Reitmaier, B. Wittmann, V. V. Bel'kov, E. L. Ivchenko, Z. D. Kvon, N. Q. Vinh, A. F. G. van der Meer, B. Murdin, and S. D. Ganichev, Phys. Rev. B **77**, 245304 (2008).

[72] M. Otteneder, S. Hubmann, X. Lu, D. A. Kozlov, L. E. Golub, K. Watanabe, T. Taniguchi, D. K. Efetov, and S. D. Ganichev, Nano Lett. **20**, 7152 (2020).

[73] E. L. Ivchenko and G. E. Pikus, *Superlattices and Other Heterostructures* (Springer, Berlin, Heidelberg, 1997).

[74] E. L. Ivchenko, *Optical Spectroscopy of Semiconductor Nanostructures* (Alpha Sci. Int. Ltd., Harrow, 2005).

[75] S. D. Ganichev and W. Prettl, *Intense Terahertz Excitation of Semiconductors* (Oxford University Press, Oxford, 2005).

[76] H. Linke, T. E. Humphrey, P. E. Lindelof, A. Löfgren, R. Newbury, P. Omling, A. O. Sushkov, R. P. Taylor, and H. Xu, Appl. Phys. A **75**, 237 (2002).

[77] S. V. Koniakhin, Eur. Phys. J. B **87**, 216 (2014).

[78] L. Braun, G. Mussler, A. Hruban, M. Konczykowski, T. Schumann, M. Wolf, M. Münzenberg, L. Perfetti, and T. Kampfrath, Nat. Commun. **7**, 13259 (2016).

[79] K. W. Kim, T. Morimoto, and N. Nagaosa, Phys. Rev. B **95**, 035134 (2017).

[80] H. Plank, J. Pernul, S. Gebert, S. N. Danilov, J. König-Otto, S. Winnerl, M. Lanius, J. Kampmeier, G. Mussler, I. Aguilera, D. Grützmacher, and S. D. Ganichev, Phys. Rev. Mater. **2**, 024202 (2018).

[81] H. Plank and S. D. Ganichev, Solid-State Electron. **147**, 44 (2018).

[82] N. V. Leppenen and L. E. Golub, Phys. Rev. B **107**, L161403 (2023).

[83] M. M. Glazov and L. E. Golub, Phys. Rev. B **102**, 155302 (2020).

[84] Note that the traces were obtained from two separated arrays with identical parameters, which, however, may have slightly different characteristics; see Fig. 10 in Appendix A.